

# OA-BEV: Bringing Object Awareness to Bird’s-Eye-View Representation for Multi-Camera 3D Object Detection

Xiaomeng Chu<sup>1</sup> Jiajun Deng<sup>2\*</sup> Yuan Zhao<sup>1</sup> Jianmin Ji<sup>1</sup> Yu Zhang<sup>1</sup>  
Houqiang Li<sup>1</sup> Yanyong Zhang<sup>1\*</sup>

<sup>1</sup> University of Science and Technology of China (USTC)

<sup>2</sup> The University of Sydney (USYD)

## Abstract

The recent trend for multi-camera 3D object detection is through the unified bird’s-eye view (BEV) representation. However, directly transforming features extracted from the image-plane view to BEV inevitably results in feature distortion, especially around the objects of interest, making the objects blur into the background. To this end, we propose OA-BEV, a network that can be plugged into the BEV-based 3D object detection framework to bring out the objects by incorporating object-aware pseudo-3D features and depth features. Such features contain information about the object’s position and 3D structures. First, we explicitly guide the network to learn the depth distribution by object-level supervision from each 3D object’s center. Then, we select the foreground pixels by a 2D object detector and project them into 3D space for pseudo-voxel feature encoding. Finally, the object-aware depth features and pseudo-voxel features are incorporated into the BEV representation with a deformable attention mechanism. We conduct extensive experiments on the nuScenes dataset to validate the merits of our proposed OA-BEV. Our method achieves consistent improvements over the BEV-based baselines in terms of both average precision and nuScenes detection score. Our codes will be published.

## 1. Introduction

Multi-view cameras have become one of the mainstream sensors for 3D object detection in autonomous driving [1, 30, 37], thanks to their comprehensive perceptive capability of the entire scope at very low price points. To achieve precise 3D object detection, the recent trend is to convert the image features to the bird’s-eye view (BEV) and then to perform detection subsequently. The following two advantages account for this trend. First, performing 3D object detection

\*Corresponding Author: Jiajun Deng and Yanyong Zhang.

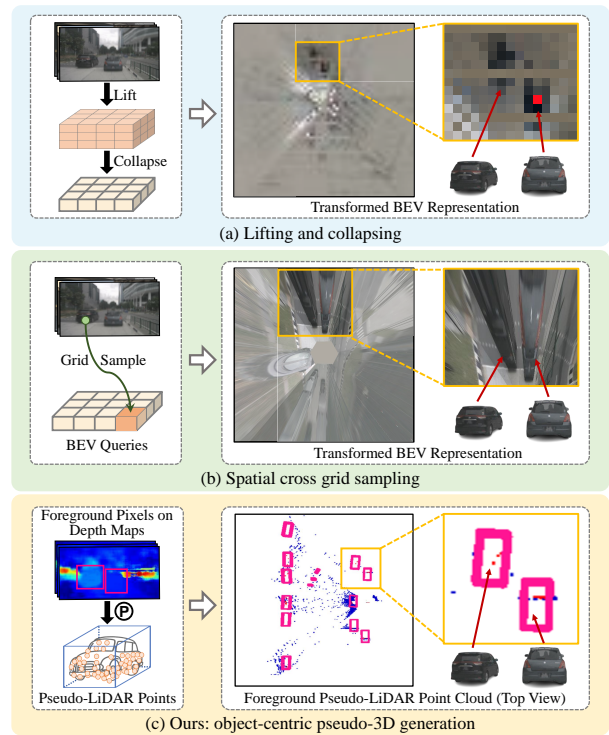


Figure 1. The comparison and visualization of different view transformation methods. (a) The lifting-collapsing method. (b) Spatial cross sampling method. The sampling locations are determined via geometric projection only without attention mechanism. (c) The object-centric pseudo-3D generation method.

on BEV is especially advantageous due to the absence of occlusion and perspective distortion. Second, BEV’s ability to represent the panoramic driving scenes lends it well to jointly reasoning about multiple tasks [49] and fusing perception data from different views, modalities, and time series into a unified view [12, 25, 32].

The core step of BEV-based 3D object detection is the

transformation of features from the image-plane view to the BEV. The existing methods either lift image pixels to a 3D frustum following the geometric principles and then spat them onto the BEV plane [13, 20], or form the target grid-shaped BEV queries by sampling image features via attention mechanisms [14, 21]. These methods equally treat all pixels, regardless of whether a pixel belongs to an object or not. No particular attention is given to pixels that belong to objects of interest. However, when converting image features to the BEV plane, feature distortion is inevitable. The deformed BEV representation blurs the boundaries between the objects and the background, making it difficult for the network to distinguish them. We explain our points with examples in Figure 1. The foremost observation is that, whether it is (a) the lifting-collapsing method [36] or (b) the spatial cross grid sampling method [21], the image-plane features are deformed (boxed in the BEV maps) during view transformation, making it difficult to accurately identify the objects. Inaccurate BEV features, especially those that describe the objects, will affect the detection ability of the BEV detection head. At the same time, the direct transformation from the features extracted in the image plane will lead to the lack of the 3D structure, especially for the foreground objects.

To address these challenges, in this work, we aim to extract features that can give additional cues to the object’s 3D spatial information. In particular, we focus on two such features. The first one is the object’s depth information we can estimate from the original images, and the second one is the foreground pseudo-point cloud (*e.g.* object-centric pseudo-3D representation) we can obtain by combining the object locations on images and the estimated depth maps. These two features provide additional 3D spatial information for each object, and by fusing them with the BEV features we can enhance the spatial details of the objects. Thus, the detection system becomes more *object aware*. Formally, we introduce OA-BEV, which devises such a branch to enhance the BEV-based 3D object detection by harvesting the object-aware 3D information as explained above.

In generating these two object-aware spatial features, the main issue is not to utilize any extra depth labels. As such, we supervise all pixels in the foreground regions of multi-camera images with the object’s center point location to obtain the estimated depth maps [47]. Next, we apply a 2D detector and use the predicted 2D bounding boxes on the depth maps to select the foreground regions. Then, we project the selected foreground depth map pixels to the 3D space to form pseudo-LiDAR point clouds [43]. From Figure 1(c), we observe that the foreground pseudo-LiDAR point clouds are indeed sparse but give a more accurate representation of the object location than the BEV representation. After performing voxelization and several layers of 3D sparse convolutions, we encode the foreground pseudo-LiDAR point

clouds as pseudo-voxel features. Finally, OA-BEV fuses the pseudo-voxel features and depth features with deformable attention.

To validate the merits of our proposed OA-BEV, we evaluate the proposed OA-BEV on the challenging nuScenes [3] benchmark. Plugged in with two baseline networks BEVDet [13] and BEVFormer [21], OA-BEV can help achieve consistent improvements. Remarkably, OA-BEV achieves 43.1% mAP and 52.8% NDS on the val set, outperforming BEVFormer by 1.5% and 1.1%, respectively. Our method reaches 49.4% mAP and 57.5% NDS, respectively, on the test set without bells and whistles.

In summary, our main contributions are as follows:

- We propose OA-BEV, a plug-in module that brings better object awareness with regard to their 3D spatial properties to the BEV representation for multi-camera 3D object detection, thereby compensating for feature deformation as well as 3D structure missing in BEV view transformation.
- We generate object-aware features by reusing 3D object detection labels, without introducing extra depth annotation. We also show that such lightweight operations can lead to considerable improvements.
- We conduct experiments with two representative baselines, *i.e.*, BEVFormer and BEVDet, with multiple backbones on the nuScenes dataset. With OA-BEV plugged in, the performance improvements in both methods verify the utility of our approach.

## 2. Related work

In this section, we give a brief review of visual 3D object detection, including monocular 3D object detection, stereo 3D object detection and multi-camera 3D object detection.

**Monocular 3D Object Detection:** Taking a monocular image as input, there are two types of 3D object detection methods, one supervises the network only with the attributes of a 3D object [2, 18, 33, 47, 48], and the other uses extra data such as depth or semantic labels [6, 29, 31, 38]. We present examples of both types of methods below. FCOS3D [41] is a single-stage 3D object detector that predicts the 7-DoF properties of 3D objects in images. SMOKE [26] constructs the 3D bounding box by combining a single keypoint estimate with regressed 3D variables for 8 box corners. Ding et al. [8] proposed a novel local convolutional network, where the filters are generated from the depth map dynamically. Y. Wang et al. [43] proposed “Pseudo-LiDAR”, which is obtained from the combination of image pixel coordinates and corresponding depth.

**Stereo 3D Object Detection:** Stereo images can utilize the corresponding relationship of pixels between left and right inputs to recover 3D information [4, 10, 46]. Stereo R-CNN [17] proposes a left-right photometric alignment for

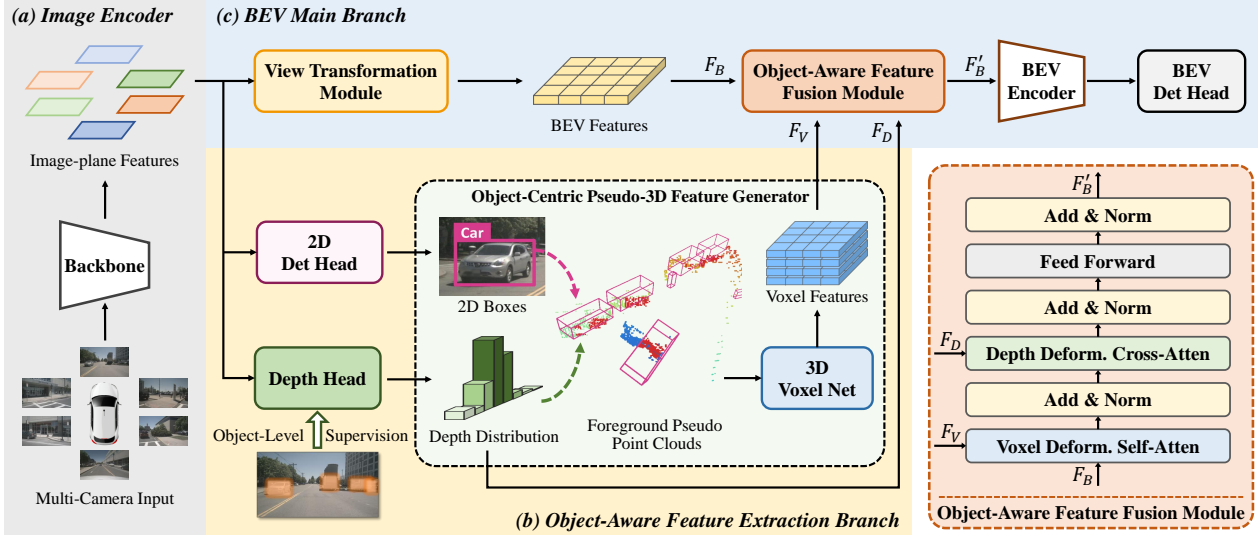


Figure 2. Overview of the OA-BEV framework. (a) The multi-camera images are input to the backbone network to extract the image-plane 2D features. (b) In the object-aware feature extraction branch, the image-plane features are fed into a 2D detection head and a depth head with the object-level supervision. After softmax on the depth features  $F_D$ , the depth maps and 2D detection bounding boxes are combined in the object-centric pseudo-3D feature generator to project foreground pseudo-LiDAR point clouds, which is encoded into voxel features  $F_V$  via a 3D voxel network. (c) In the BEV main branch, the image features are input into the view transformation module to obtain the BEV features  $F_B$ , which are fused with the depth features  $F_D$  and voxel features  $F_V$  via an object-aware feature fusion module. The updated BEV features  $F'_B$  are further fed into a BEV encoder and a BEV detection head. The bottom right part shows the details of the object-aware feature fusion module, which is mainly composed of a voxel deformable self-attention and depth deformable cross-attention.

more precise depth prediction, and combines the 2D detection bounding boxes and keypoints to geometrically predict the 3D position. DSGN [5] constructs a plane-sweep volume by concatenating the aligned stereo image features and the depth values of corresponding pixels. Disp R-CNN [39] learns depth information and semantic cues simultaneously and predicts instance-level disparity to generate instance point clouds.

**Multi-Camera 3D Object Detection:** Providing a panoramic view, multi-camera 3D object detection, which can be divided into two categories: image-view-based [23, 34, 44] and BEV-based [13, 19–21, 35, 50], has attracted extensive attention in recent years. DETR3D [44] and PETR [23] involve the deformable transformer [52] into this task, where the former uses 3D object queries to index 2D feature points, and the latter embeds the 3D position information into the 2D features. BEVDet [13] constructs BEV features via the lifting-collapsing method and performs feature extraction in both image view space and BEV space. BEVFormer [21] extracts the spatial features across camera views through deformable cross attention [52]. It also aggregates temporal information, which has been proven by many recent methods [12, 14, 19, 35] to be effective in improving detection performance.

### 3. Methodology

#### 3.1. Overview

**3D Detection with OA-BEV:** Figure 2 depicts our OA-BEV pipeline. It can function as a plugin to incorporate the object-aware features – namely, the object-level depth estimations and foreground pseudo-3D features – into any BEV-based multi-camera 3D detection pipeline. With OA-BEV plugged in, the resulting object-aware BEV-based detection usually consists of an image encoder followed by two branches: (1) the object-aware feature extraction branch and (2) the BEV main branch. The former includes three modules: (i) 2D detection head, (ii) depth head, and (iii) object-centric pseudo-3D feature generator. The latter consists of four modules: (i) view transformation module, (ii) object-aware feature fusion module, (iii) BEV encoding module, and (iv) BEV detection head. Sometimes, the BEV encoding module is not required.

The actual workflow can be summarized as follows. First, we input the multi-camera images to the backbone networks to extract the image features, and then feed the features into the following three modules: the view transformation module in the BEV main branch to obtain BEV features, the 2D detection head to predict 2D bounding boxes and the depth head to estimate depth maps with the object-level supervision. The latter two modules are part of the object-aware feature extraction branch. Second, the depth-

map pixels selected by the 2D bounding boxes are projected into the 3D space to form foreground pseudo-point clouds, from which object-level voxel features can be encoded by a 3D voxel network, *e.g.*, feature encoding in the 3D space. The object-level depth features and pseudo-voxel features are fused with the BEV features via deformable attention modules. Finally, the enhanced BEV features are fed into a BEV encoder and a BEV head for 3D object detection.

**Design Overview of OA-BEV:** The key modules of the proposed OA-BEV are as follows:

- (1) Depth Estimation with Object-Level Supervision. This module is to explicitly guide the network to learn the depth information, as well as to avoid the need for extra annotations. We use the ground truth depth of a 3D object as the depth value of all the pixels in the corresponding 2D bounding box (defined as the foreground region) on the images.
- (2) Object-Centric Pseudo-3D Feature Generation. This module is to construct a foreground pseudo-3D representation to encode features describing objects of interest in the 3D space. We select the pixels on the depth maps that belong to an object’s 2D bounding box and project them to 3D space to generate the pseudo-point clouds. After voxelization, we encode the pseudo-voxel features by layers of 3D sparse convolutions. This process is trained end-to-end.
- (3) Object-Aware Feature Fusion. This module is to fuse the two object-aware features into the BEV representation through deformable attention.

In the rest of this section, we discuss these modules in detail.

### 3.2. Depth Estimation with Object-Level Supervision

Without depth labels from LiDAR point clouds, depth information during view transformation is often learned implicitly [13]. In OA-BEV, we use the depth of a 3D object as the object-level supervision of the corresponding foreground region on the image [47]. That is, all the pixels within the object’s 2D bounding box share the same depth. Although our approach only provides an approximation, this explicit supervision still plays an important role in the subsequent pseudo-3D representation construction and extraction. For better prediction, we divide the depth range into intervals of unequal length and treat each interval as a class, thus modeling depth estimation as a classification problem. Specifically, the depth range  $[d_{min}, d_{max}]$  is discretized in a linearly-increasing discretization (LID) strategy [38] with a bin size of  $\sigma$  as follows:

$$\delta = \frac{2(d_{max} - d_{min})}{K(K + 1)}, \quad (1)$$

$$\hat{l} = \lfloor -0.5 + 0.5\sqrt{1 + \frac{8(\hat{d} - d_{min})}{\delta}} \rfloor,$$

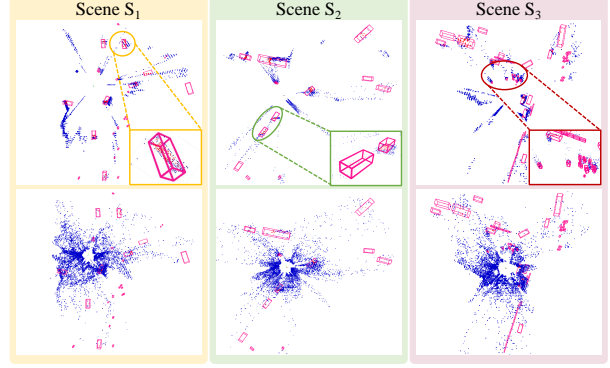


Figure 3. The comparison between the foreground pseudo-LiDAR points (top) and all points including background ones (bottom).

where  $K$  is the number of depth bins, and  $\hat{l}$  is the bin index.

As such, the depth estimation problem is viewed as a classification problem with  $K$  classes. What makes our problem unique is that the depth categories are not independent, but rather follow a natural order. Therefore, we solve the depth classification problem in an ordinal regression way [9]. In detail, the depth head outputs the feature map  $y$  of size  $H \times W \times K \times 2$ , and then, the depth probability distribution  $P$  with coordinate  $(w, h)$  is obtained by applying a softmax on  $y_{(w,h)}$  as follows:

$$P_{(w,h)}^l = \text{softmax}(y_{(w,h)}^l), \quad (2)$$

where  $P_{(w,h,0)}^l$  denotes the probability for the depth category being between  $l$  and  $K$ . We count the number of activated bins whose probability is higher than 0.5 as the depth category  $d_c$ . The median value of the  $d_c$ -th bin is used as the depth value  $d_{(w,h)}$  (in meters). It is worth noting that in an LSS-like method, the depth distribution  $\Gamma$  of size  $W \times H \times K$  is calculated as:

$$\Gamma_{(w,h)}^l = P_{(w,h,0)}^l - P_{(w,h,0)}^{l-1}. \quad (3)$$

### 3.3. Object-Centric Pseudo-3D Feature Generation

Here, we discuss how to generate pseudo-3D features that can help provide important 3D spatial information. After obtaining the depth maps, we integrate the 2D object detector FCOS [40] into our pipeline to predict 2D bounding boxes on multi-camera images. All the pixels within the bounding boxes are considered foreground pixels. We only use foreground pixels on depth maps in the subsequent steps to focus on the objects of interest. In the implementation, after the image encoder, we insert an FPN [22] and a 2D object detection head as the 2D object detector. We then combine the selected pixels’ coordinates  $(u, v)$  with the corresponding depth to generate a pseudo-LiDAR point  $(x, y, z)$ . The transformation can be formulated as follows:

$$x = \frac{(u - c_x)z}{f_x}, \quad y = \frac{(v - c_y)z}{f_y}, \quad z = D(u, v), \quad (4)$$

where  $(c_x, c_y)$  is the camera center in image pixel location, and  $z$  is the pixel’s estimated depth output by the depth head  $D$ . As shown in Figure 3, the pseudo-point clouds with the background points removed can better describe the objects’ spatial properties such as location and 3D structure, hence object-centric. We train the 2D object detector together with 3D object detection in an end-to-end manner.

To balance accuracy and efficiency, we adopt the voxel-based 3D feature encoder instead of the point-based. After the pseudo-point cloud voxelization, the 3D space is represented as a sparse 4D tensor with the size of  $(H_{BEV}, W_{BEV}, Z, C)$ . The voxel features  $F_V$  are extracted through multi-layer 3D sparse convolutions. We can further flatten the voxel features along the  $z$ -axis to convert them into BEV features with the size of  $(H_{BEV}, W_{BEV}, Z \cdot C)$ .

### 3.4. Object-Aware Feature Fusion

Finally, we need to aggregate the two types of object-aware features – i.e., the pseudo-3D feature  $F_V$  (flattened into BEV) and the depth feature  $F_D$  – with the BEV features  $F_B$ . Deformable attention [52] is an effective way to establish soft associations between features that are not aligned. Considering the positional and semantic misalignment between the object-aware features and BEV features, we engage the deformable transformer to fuse them.

The sparse 3D convolutions render the resulting voxel features only have valid values in those grids that are covered by the pseudo-LiDAR points. Therefore, there are a large number of invalid grids in  $F_V$ . In order to save memory, we use the valid values in  $F_V(p)$  as queries, and take the BEV features  $F_B$  as the values. Then, we replace the values at the corresponding position in  $F_B$  with the ones calculated by the voxel deformable self-attention (VSA) to obtain the BEV output  $O_p$  located at  $p = (x, y)$ :

$$\mathcal{VSA}(F_V(p), F_B) = DA(F_V(p), p, F_B), \quad (5)$$

$$\begin{cases} \mathcal{VSA}(F_V(p), F_B), & \text{if } F_V(p) \text{ is valid,} \\ F_B(p), & \text{if } F_V(p) \text{ is invalid,} \end{cases} \quad (6)$$

where  $DA$  denotes deformable attention. In this way, we can aggregate the foreground pseudo-3D features into the BEV representation.

To take full advantage of the object-level depth estimation, we conduct deformable spatial cross attention [21] on the multi-camera depth maps. We take the depth features  $F_D$  before softmax as the value, and evenly select  $N_{ref}$  3D reference points in the pillar of each BEV query  $Q_p$ , thereby projecting them to the selected depth feature maps  $\Gamma'_h$  for sampling. The weighted sum is calculated for all depth feature points sampled by  $Q_p$ . The process of depth deformable cross attention (DCA) can be formulated as:

$$DCA(Q_p, F_D) = \frac{1}{|\Gamma'_h|} \sum_{i \in \Gamma'_h} \sum_{j=1}^{N_{ref}} DA(Q_p, \mathcal{M}(p, i, j), F_D^i), \quad (7)$$

where  $\mathcal{M}$  is the camera’s projection matrix.

### 3.5. Loss Function

Our loss function has three parts: (1) the 3D object detection loss  $L_{3D}$ , (2) the 2D object detection loss  $L_{2D}$ , and (3) the foreground depth classification loss  $L_{dep}$ . As such, it can be calculated as follows:

$$Loss = \alpha \cdot L_{3D} + \beta \cdot L_{2D} + \gamma \cdot L_{dep}, \quad (8)$$

where  $\alpha$ ,  $\beta$ , and  $\gamma$  are the weight coefficients of the three types of loss, respectively. When training, we adjust these coefficients so that the three types of losses are roughly kept at a ratio of 20:4:1.  $L_{dep}$  is defined as the average ordinal loss of all foreground pixels in predicted depth distributions:

$$L_{dep} = \frac{1}{N} \sum_{n=0}^{N-1} \left( \sum_{k=0}^{l_{n-1}} \log P_{(n,0)}^k + \sum_{k=l_n}^K \log P_{(n,1)}^k \right), \quad (9)$$

where the product  $N < H \times W$  denotes the total number of foreground pixels in the depth map, and  $K$  is the number of discretized depth intervals.

## 4. Experiments

### 4.1. Datasets and Metrics

We conduct experiments on the large-scale autonomous driving dataset nuScenes [3] which covers a variety of perception tasks, such as detection, tracking, and LiDAR segmentation, etc. The nuScenes dataset consists of 1000 scenes, which are divided into 700, 150, and 150 scenes for training, validation, and testing, respectively. Each scene contains 20s of perceptual data, annotated with a keyframe at 2Hz. The data acquisition vehicle is equipped with one LiDAR, five radars, and six cameras that form a surround view. For 3D object detection benchmarks, nuScenes proposes several true positive metrics to measure the detection errors, the lower the better. Especially, ATE, ASE, AOE, AVE, and AAE are used to evaluate translation, scale, orientation, velocity, and attribute errors, respectively. In addition, the mean average precision (mAP) and the nuScenes detection score (NDS) are two comprehensive metrics used to measure the detection performance, the higher the better.

### 4.2. Implementation Details

For experiments on nuScenes, the BEV perception range is  $[-51.2m, 51.2m]$  for  $X$  and  $Y$  axes and  $[-5m, 3m]$  for  $Z$  axis. We evaluate the average detection results for ten categories including car, truck, bicycle, pedestrian, etc.

**Implementation Details of Baseline Models.** To evaluate the effect of object-aware features, we adopt OA-BEV on two baselines, namely BEVDet [13] and BEVFormer [21]. We name our models based on the above two networks *OA-BEVDet* and *OA-BEVFormer*, respectively.

Table 1. Comparison of different paradigms on the nuScenes val set. ST denotes Swin-Transformer [24]. § is initialized from ST-Tiny pre-trained on the nulmages. † is initialized from a FCOS3D backbone. \* notes that VoVNet-99 (V2-99) [15] was pre-trained with external data [34]. ‡ fine-tuned and tested with test time augmentation. The DETR3D, PETR and BEVDet are trained with CBGS [51].

Methods	Image Size	Backbone	mAP↑	NDS↑	mATE↓	mASE↓	mAOE↓	mAVE↓	mAAE↓
BEVDet-T [13]	704×256	ST-tiny	0.294	0.384	0.686	0.278	0.547	0.865	0.261
OA-BEVDet-T§	704×256	ST-tiny	<b>0.342</b>	<b>0.411</b>	0.666	0.273	0.520	0.882	0.265
BEVFormer-S† [21]	1280×720	R-101	0.389	0.492	0.700	0.275	0.390	0.424	0.196
OA-BEVFormer-S†	1280×720	R-101	<b>0.407</b>	<b>0.510</b>	0.687	0.271	0.375	0.416	0.193
FCOS3D‡ [41]	1600×900	R-101	0.343	0.415	0.725	0.263	0.422	1.292	0.153
DETR3D† [44]	1600×900	R-101	0.349	0.434	0.716	0.268	0.379	0.842	0.200
PGD‡ [42]	1600×900	R-101	0.369	0.428	0.683	0.260	0.439	1.268	0.185
PETR† [23]	1600×900	R-101	0.370	0.442	0.711	0.267	0.383	0.865	0.201
MonoDETR† [47]	1600×900	R-101	0.372	0.434	0.676	0.258	0.429	1.253	0.176
BEVDet† [13]	1600×640	V2-99*	0.390	0.459	0.602	0.258	0.382	0.901	0.216
OA-BEVDet†	1600×640	V2-99*	<b>0.402</b>	<b>0.465</b>	0.597	0.252	0.355	0.932	0.220
BEVFormer† [21]	1600×900	R-101	0.416	0.517	0.673	0.274	0.372	0.394	0.198
OA-BEVFormer†	1600×900	R-101	<b>0.431</b>	<b>0.528</b>	0.664	0.272	0.388	0.345	0.205

Table 2. Comparison with the state-of-the-art methods on the nuScenes test set. \* notes that VoVNet-99 (V2-99) [15] was pre-trained on the depth estimation task with extra data [34]. ‡ is test time augmentation.

Methods	Image Size	Backbone	mAP↑	NDS↑	mATE↓	mASE↓	mAOE↓	mAVE↓	mAAE↓
FCOS3D‡ [41]	1600×900	R-101	0.358	0.428	0.690	0.249	0.452	1.434	0.124
PGD‡ [42]	1600×900	R-101	0.386	0.448	0.626	0.245	0.451	1.509	0.127
BEVDet [13]	1600×640	ST-Small	0.398	0.463	0.556	0.239	0.414	1.010	0.153
DETR3D [44]	1600×900	V2-99*	0.412	0.479	0.641	0.255	0.394	0.845	0.133
DD3D‡ [34]	1600×900	V2-99*	0.418	0.477	0.572	0.249	0.368	1.014	0.124
PETR [23]	1600×900	V2-99*	0.441	0.504	0.593	0.249	0.383	0.808	0.132
BEVFormer [21]	1600×900	R-101	0.445	0.535	0.631	0.257	0.405	0.435	0.143
BEVDet4D‡ [12]	1600×900	ST-Base	0.451	0.569	0.511	0.241	0.386	0.301	0.121
BEVFormer [21]	1600×900	V2-99*	0.481	0.569	0.582	0.256	0.375	0.378	0.126
OA-BEV	1600×900	V2-99*	<b>0.494</b>	<b>0.575</b>	0.574	0.256	0.377	0.385	0.132

BEVDet adopts SwinTransformer-Tiny [24] and ResNet101 [11] as the backbones for the tiny and base versions, followed by an FPN-LSS. The input resolutions are set to  $704 \times 256$  and  $1600 \times 640$  for the two versions, respectively. This BEV-based pipeline takes lifting-collapsing [36] as the view transformation method, the combination of a lightweight ResNet and an FPN as the BEV encoder, and CenterHead [45] as the BEV detection head. In view transformation, BEVDet divides the ground plane with a resolution of 0.4 meters for the base version and 0.8 meters for the tiny version. BEVFormer-Small adopts ResNet101-DCN [7, 11] as the backbone. For base version, it conducts experiments with both ResNet101-DCN and VoVNet-99 [15] as backbones. The input resolutions are set to  $1280 \times 720$  and  $1600 \times 900$  for the two versions, respectively. It performs view transformation through stacked of spatial cross-attention layers, and takes the DETR head [44] as the BEV detection head. In view transformation, BEVFormer-Base sets the size of BEV queries to  $200 \times 200$ . To maintain the same size as the output of 3D voxel network in OA-BEV, we set the size

of BEV queries to  $160 \times 160$  for BEVFormer-Small. In addition, BEVFormer aggregates temporal features to recurrently fuse the history BEV information.

**Implementation Details of OA-BEV.** As mentioned before, we choose BEVDet [13] and BEVFormer [21] with a general pipeline as the baseline to verify the effect of object awareness on the BEV-based multi-camera 3D object detection task. We set up three versions of OA-BEV: tiny, small, and base, with different input resolutions, backbones, feature dimensions, and sizes of BEV grids.

The key modules attached to the general pipeline in OA-BEV include a 2D objection head, a depth head with object-level supervision, an object-centric pseudo-3D feature generator, and an object-aware feature fusion module. To select foreground regions, we insert an FPN with 256 channels and an FCOS head after the backbone to predict the 2D bounding boxes. The depth head is lightweight and consists of only one layer of convolution with  $K \times 2$  channels followed by a softmax, where  $K = 80$  is the number of depth bins in our network. In the object-centric pseudo-3D feature

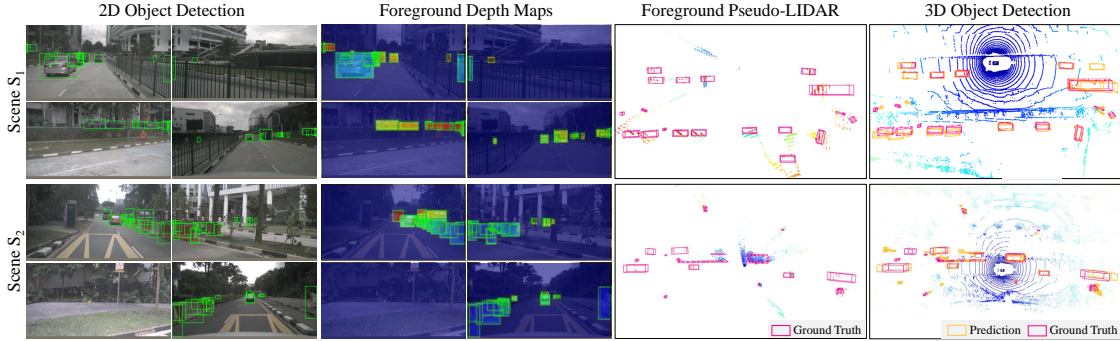


Figure 4. Visualization of the OA-BEV pipeline. From left to right are the 2D object detection results, foreground depth maps selected by 2D bounding boxes, foreground pseudo-LiDAR point clouds, and the final 3D object detection results shown on the BEV.

generator, we select the foreground pixels in depth maps with the predicted 2D bounding boxes, and use the camera intrinsics and extrinsics to generate the foreground 3D pseudo-LiDAR point clouds. In the next step, the pseudo point clouds are voxelized and then fed to a voxel network composed of 4 layers of 3D sparse convolutions to obtain an  $8\times$  downsampled volume. We flatten the volume along the  $z$ -axis to obtain a BEV output. For the object-aware feature fusion module, we use 3 encoder layers, each following the conventional structures of deformable transformer [52]. The attention layers are replaced with the voxel deformable self attention and the depth deformable cross attention.

**Training.** We broadly follow the training strategies of the two baselines. All models are trained for 24 epochs with AdamW [28] optimizer and a learning rate of  $2e-4$ . The learning rate multiplier of VoVNet-99 [16] and ResNet-101 [11] as the backbone for the base version is 0.1. With BEVDet as the baseline, we train the model with a batch size of 1 per GPU on 10 NVIDIA GeForce RTX 3090 GPUs. With BEVFormer as the baseline, we decay the learning rate with a cosine annealing [27], a batch size of 1 per GPU on 8 NVIDIA GeForce RTX A6000 GPUs. We train the entire model in an end-to-end manner.

### 4.3. Performance Comparison on nuScenes Dataset

Using nuScenes val set and test set, we compare OA-BEV with the current state-of-the-art multi-camera 3D perception methods. All of the methods use images as input and ground-truth 3D objects as supervision when training.

Let us first look at the val set results that are shown in Table 1. Here, we have four groups of comparison experiments because we validate our plug-in module on two baselines and set up two versions of each.

In the first group, we compare the performance of the tiny version between OA-BEVDet and BEVDet. The two networks share the same backbone SwinTransformer-Tiny with a low input resolution of  $704 \times 256$ . Besides, the

BEV features with a small size of  $128 \times 128$  improve efficiency but also reduce its ability to describe the objects due to the coarse granularity. OA-BEVDet-Tiny significantly surpasses BEVDet on mAP and NDS by 3.8% and 2.7%, respectively, which shows that the object-aware features have a pronounced effect on poor BEV representations.

Due to the use of temporal information, the performance of BEVFormer [21] is significantly improved compared to that of BEVDet, especially the lower mAVE. In the second and fourth groups, we compare the performance of small and base versions between OA-BEVFormer and BEVFormer, respectively. Without any modification to the use of temporal information, OA-BEVFormer-Small outperforms BEVFormer-Small on both mAP and NDS by 1.8%, while OA-BEVFormer outperforms BEVFormer on mAP and NDS by 1.5% and 1.1% for the base version. All the methods in the third group perform multi-camera 3D object detection without the data fusion of time series. We reproduce the performance of BEVDet-Base with VoVNet-99 as the backbone and take this as the baseline to verify the effect of object-aware features. OA-BEVDet achieves improvements of 1.2% and 0.6% on mAP and NDS, respectively. Comparing the performance improvements of OA-BEV in different settings, we note that the object-aware features play a greater role when the original BEV representation has lower quality.

The changes of mAP in the training process for OA-BEV with BEVDet-Tiny and BEVFormer-Small are shown in Figure 5. We observe that our method shows advantages early in training and converges faster.

Table 2 summarizes the test set results. For the results on the test set, we take the BEVFormer as the baseline and train the models on both train set and val set. Without any test time augmentation or model ensemble, OA-BEV surpasses BEVFormer with VoVNet-99 by 1.3% in mAP and 0.6% in NDS, respectively. From the above results, we conclude that OA-BEV can consistently improve the detection performance in terms of mAP and NDS when combined with

Table 3. Ablation study for the data augmentation strategy on the nuScenes *val* set. ODS denotes Object-level Depth Supervision. DF denotes Depth Feature Fusion. PF denotes Pseudo-3D Feature Fusion. P<sub>null</sub> denotes that the backbone was pre-trained on nuImages.

ID	ODS	DF	PF	P <sub>null</sub>	mAP↑	NDS↑	mATE↓	mASE↓	mAOE↓	mAVE↓	mAAE↓
A					0.294	0.384	0.686	0.278	0.547	<b>0.865</b>	0.261
B				✓	0.312	0.390	0.711	<b>0.272</b>	0.523	0.909	<b>0.247</b>
C	✓			✓	0.326	0.398	0.708	0.275	0.531	0.884	0.254
D	✓		✓	✓	0.338	0.407	0.673	0.277	0.528	0.884	0.255
E	✓	✓	✓	✓	<b>0.342</b>	<b>0.411</b>	<b>0.666</b>	0.273	<b>0.520</b>	0.882	0.265

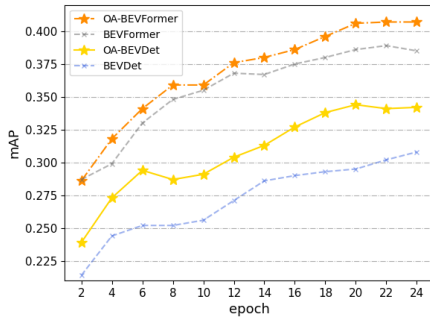


Figure 5. The evolution of mAP in the training process. We compare the intermediate results in the lightweight versions of OA-BEV and its two baseline networks.

different base models in different settings.

#### 4.4. Visualization Results

In Figure 4, we present the visualized intermediate outputs and detection results of OA-BEV in two complex scenes, including the 2D detection bounding boxes, the estimated foreground depth maps, the foreground pseudo-LiDAR point clouds, and the 3D object detection bounding boxes from left to right. From the visualization results, we observe that the foreground pseudo-point clouds provide accurate locations of the objects, which is particularly important for small and remote ones.

#### 4.5. Ablation Studies

To quantify the impact of each module on the performance of OA-BEV, we summarize the results of our ablation studies in Table 3.

**Impact of Object-Level Depth Supervision:** We supervise the foreground pixels in depth maps using the depth value of the corresponding 3D object instead of extra depth labels. Comparing the second and third rows of Table 3, we observe that the network with object-level depth supervision increases the mAP and NDS metrics by 1.4% and 0.8%, respectively. This shows that depth supervision is beneficial to the underlying detection performance of OA-BEV.

**Impact of Pseudo-3D Features:** We fuse the pseudo-3D features via voxel deformable self-attention. According to Table 3, the fusion of foreground pseudo-3D features con-

tributes to the overall detection accuracy, especially for the metric of mAP (+1.2%). This confirms the positive effect of the pseudo-3D features in assisting the network to identify objects. For more specific analysis, it can be found that OA-BEV reduces the translation error (mATE) by 0.035 but has little effect on the attribute error (mAAE). These results indicate that pseudo-3D representation, which lacks the rich semantic information compared to image features, improves detection performance by providing spatial information to help recognize the pose of objects, rather than by enhancing the semantic representation of the objects.

**Impact of Depth Features:** The depth features are fused with BEV features through depth deformable cross-attention. The comparison between the last two rows of table 3 shows the effect of fusing the depth features. It can both improve the mAP and NDS by 0.4%, and reduce most of the errors except for the attribute error. This shows that the depth distribution can not only be used in view transformation, but can also be directly encoded into the BEV representation to further improve the performance.

**Impact of nuImages Pre-training:** As can be seen from the second row of Table 3, pre-training the backbone on nuImages helps to improve performance and reduce the attribute error by 0.014. This can be attributed to the fact that pre-training on 2D perception tasks make the network pay more attention to the semantic features of images.

## 5. Conclusion

In this paper, we propose OA-BEV which can be plugged into the BEV-based multi-camera 3D object detection framework. The key innovation is to exploit the object-aware features to bring out the objects from the background, which can alleviate the deformation incurred during view transformation. That is, OA-BEV estimates the object depth map with object-level supervision and extracts the foreground pseudo-3D features, which give clear cues about the position and 3D structure of an object. By integrating these features into the BEV representation, we can obtain more descriptive features and improve their detection performance. plugged into two representative baseline networks, the consistent improvements on nuScenes demonstrate the effectiveness of our method.



## References

- [1] Eduardo Arnold, Omar Y. Al-Jarrah, Mehrdad Dianati, Saber Fallah, David Oxtoby, and Alex Mouzakitis. A survey on 3d object detection methods for autonomous driving applications. *IEEE Transactions on Intelligent Transportation Systems (T-ITS)*, 2019. [1](#)
- [2] Garrick Brazil and Xiaoming Liu. M3D-RPN: monocular 3d region proposal network for object detection. In *IEEE/CVF International Conference on Computer Vision (ICCV)*, 2019. [2](#)
- [3] Holger Caesar, Varun Bankiti, Alex H. Lang, Sourabh Vora, Venice Erin Liong, Qiang Xu, Anush Krishnan, Yu Pan, Giancarlo Baldan, and Oscar Beijbom. nuscenes: A multi-modal dataset for autonomous driving. In *IEEE/CVF Conference on Computer Vision and Pattern Recognition (CVPR)*, 2020. [2](#), [5](#)
- [4] Jia-Ren Chang and Yong-Sheng Chen. Pyramid stereo matching network. In *IEEE/CVF Conference on Computer Vision and Pattern Recognition (CVPR)*, 2018. [2](#)
- [5] Yilun Chen, Shu Liu, Xiaoyong Shen, and Jiaya Jia. DSGN: deep stereo geometry network for 3d object detection. In *IEEE/CVF Conference on Computer Vision and Pattern Recognition (CVPR)*, 2020. [3](#)
- [6] Xiaomeng Chu, Jiajun Deng, Yao Li, Zhenxun Yuan, Yanyong Zhang, Jianmin Ji, and Yu Zhang. Neighbor-vote: Improving monocular 3d object detection through neighbor distance voting. In *ACM Multimedia Conference*, 2021. [2](#)
- [7] Jifeng Dai, Haozhi Qi, Yuwen Xiong, Yi Li, Guodong Zhang, Han Hu, and Yichen Wei. Deformable convolutional networks. In *IEEE/CVF International Conference on Computer Vision (ICCV)*, 2017. [6](#)
- [8] Mingyu Ding, Yuqi Huo, Hongwei Yi, Zhe Wang, Jianping Shi, Zhiwu Lu, and Ping Luo. Learning depth-guided convolutions for monocular 3d object detection. In *IEEE/CVF Conference on Computer Vision and Pattern Recognition (CVPR)*, 2020. [2](#)
- [9] Huan Fu, Mingming Gong, Chaohui Wang, Kayhan Batmanghelich, and Dacheng Tao. Deep ordinal regression network for monocular depth estimation. In *IEEE/CVF Conference on Computer Vision and Pattern Recognition (CVPR)*, 2018. [4](#)
- [10] Xiaoyang Guo, Kai Yang, Wukui Yang, Xiaogang Wang, and Hongsheng Li. Group-wise correlation stereo network. In *IEEE/CVF Conference on Computer Vision and Pattern Recognition (CVPR)*, 2019. [2](#)
- [11] Kaiming He, Xiangyu Zhang, Shaoqing Ren, and Jian Sun. Deep residual learning for image recognition. In *IEEE/CVF Conference on Computer Vision and Pattern Recognition (CVPR)*, 2016. [6](#), [7](#)
- [12] Junjie Huang and Guan Huang. Bevdet4d: Exploit temporal cues in multi-camera 3d object detection. *CoRR*, 2022. [1](#), [3](#), [6](#)
- [13] Junjie Huang, Guan Huang, Zheng Zhu, and Dalong Du. Bevdet: High-performance multi-camera 3d object detection in bird-eye-view. *CoRR*, 2021. [2](#), [3](#), [4](#), [5](#), [6](#)
- [14] Yanqin Jiang, Li Zhang, Zhenwei Miao, Xiatian Zhu, Jin Gao, Weiming Hu, and Yu-Gang Jiang. Polarformer: Multi-camera 3d object detection with polar transformers. *CoRR*, 2022. [2](#), [3](#)
- [15] Youngwan Lee, Joong-Won Hwang, Sangrok Lee, Yuseok Bae, and Jongyoul Park. An energy and gpu-computation efficient backbone network for real-time object detection. In *IEEE/CVF Conference on Computer Vision and Pattern Recognition Workshops (CVPR Workshops)*, 2019. [6](#)
- [16] Youngwan Lee, Joong-Won Hwang, Sangrok Lee, Yuseok Bae, and Jongyoul Park. An energy and gpu-computation efficient backbone network for real-time object detection. In *IEEE/CVF Conference on Computer Vision and Pattern Recognition Workshops (CVPR Workshops)*, 2019. [7](#)
- [17] Peiliang Li, Xiaozhi Chen, and Shaojie Shen. Stereo R-CNN based 3d object detection for autonomous driving. In *IEEE/CVF Conference on Computer Vision and Pattern Recognition (CVPR)*, 2019. [2](#)
- [18] Peixuan Li, Huaici Zhao, Pengfei Liu, and Feidao Cao. RTM3D: real-time monocular 3d detection from object keypoints for autonomous driving. In *European Conference on Computer Vision (ECCV)*, 2020. [2](#)
- [19] Yinhao Li, Han Bao, Zheng Ge, Jinrong Yang, Jianjian Sun, and Zeming Li. Bevstereo: Enhancing depth estimation in multi-view 3d object detection with dynamic temporal stereo. *CoRR*, 2022. [3](#)
- [20] Yinhao Li, Zheng Ge, Guanyi Yu, Jinrong Yang, Zengran Wang, Yukang Shi, Jianjian Sun, and Zeming Li. Bevdepth: Acquisition of reliable depth for multi-view 3d object detection. *CoRR*, 2022. [2](#), [3](#)
- [21] Zhiqi Li, Wenhai Wang, Hongyang Li, Enze Xie, Chonghao Sima, Tong Lu, Yu Qiao, and Jifeng Dai. Bevformer: Learning bird’s-eye-view representation from multi-camera images via spatiotemporal transformers. In *European Conference on Computer Vision (ECCV)*, 2022. [2](#), [3](#), [5](#), [6](#), [7](#)
- [22] Tsung-Yi Lin, Piotr Dollár, Ross B. Girshick, Kaiming He, Bharath Hariharan, and Serge J. Belongie. Feature pyramid networks for object detection. In *IEEE/CVF Conference on Computer Vision and Pattern Recognition (CVPR)*, 2017. [4](#)
- [23] Yingfei Liu, Tiancai Wang, Xiangyu Zhang, and Jian Sun. PETR: position embedding transformation for multi-view 3d object detection. In *European Conference on Computer Vision (ECCV)*, 2022. [3](#), [6](#)
- [24] Ze Liu, Yutong Lin, Yue Cao, Han Hu, Yixuan Wei, Zheng Zhang, Stephen Lin, and Baining Guo. Swin transformer: Hierarchical vision transformer using shifted windows. In *IEEE/CVF International Conference on Computer Vision (ICCV)*, 2021. [6](#)
- [25] Zhijian Liu, Haotian Tang, Alexander Amini, Xinyu Yang, Huizi Mao, Daniela Rus, and Song Han. Bevfusion: Multi-task multi-sensor fusion with unified bird’s-eye view representation. *CoRR*, 2022. [1](#)
- [26] Zechen Liu, Zizhang Wu, and Roland Tóth. SMOKE: single-stage monocular 3d object detection via keypoint estimation. In *IEEE/CVF Conference on Computer Vision and Pattern Recognition (CVPR Workshops)*, 2020. [2](#)
- [27] Ilya Loshchilov and Frank Hutter. SGDR: stochastic gradient descent with warm restarts. In *International Conference on Learning Representations (ICLR)*, 2017. [7](#)

- [28] Ilya Loshchilov and Frank Hutter. Decoupled weight decay regularization. In *International Conference on Learning Representations (ICLR)*, 2019. 7
- [29] Xinzhu Ma, Shinan Liu, Zhiyi Xia, Hongwen Zhang, Xingyu Zeng, and Wanli Ouyang. Rethinking pseudo-lidar representation. In *European Conference on Computer Vision (ECCV)*, 2020. 2
- [30] Xinzhu Ma, Wanli Ouyang, Andrea Simonelli, and Elisa Ricci. 3d object detection from images for autonomous driving: A survey. *CoRR*, 2022. 1
- [31] Xinzhu Ma, Zihui Wang, Haojie Li, Pengbo Zhang, Wanli Ouyang, and Xin Fan. Accurate monocular 3d object detection via color-embedded 3d reconstruction for autonomous driving. In *IEEE/CVF International Conference on Computer Vision (ICCV)*, 2019. 2
- [32] Yuexin Ma, Tai Wang, Xuyang Bai, Huitong Yang, Yuenan Hou, Yaming Wang, Yu Qiao, Ruigang Yang, Dinesh Manocha, and Xinge Zhu. Vision-centric BEV perception: A survey. *CoRR*, 2022. 1
- [33] Arsalan Mousavian, Dragomir Anguelov, John Flynn, and Jana Kosecka. 3d bounding box estimation using deep learning and geometry. In *IEEE/CVF Conference on Computer Vision and Pattern Recognition (CVPR)*, 2017. 2
- [34] Dennis Park, Rares Ambrus, Vitor Guizilini, Jie Li, and Adrien Gaidon. Is pseudo-lidar needed for monocular 3d object detection? In *IEEE/CVF International Conference on Computer Vision (ICCV)*, 2021. 3, 6
- [35] Jinyung Park, Chenfeng Xu, Shijia Yang, Kurt Keutzer, Kris Kitani, Masayoshi Tomizuka, and Wei Zhan. Time will tell: New outlooks and A baseline for temporal multi-view 3d object detection. *CoRR*, 2022. 3
- [36] Jonah Philion and Sanja Fidler. Lift, splat, shoot: Encoding images from arbitrary camera rigs by implicitly unprojecting to 3d. In *European Conference on Computer Vision (ECCV)*, 2020. 2, 6
- [37] Rui Qian, Xin Lai, and Xirong Li. 3d object detection for autonomous driving: A survey. *Pattern Recognit.*, 2022. 1
- [38] Cody Reading, Ali Harakeh, Julia Chae, and Steven L. Waslander. Categorical depth distribution network for monocular 3d object detection. In *IEEE/CVF Conference on Computer Vision and Pattern Recognition (CVPR)*, 2021. 2, 4
- [39] Jiaming Sun, Linghao Chen, Yiming Xie, Siyu Zhang, Qin-hong Jiang, Xiaowei Zhou, and Hujun Bao. Disp R-CNN: stereo 3d object detection via shape prior guided instance disparity estimation. In *IEEE/CVF Conference on Computer Vision and Pattern Recognition (CVPR)*, 2020. 3
- [40] Zhi Tian, Chunhua Shen, Hao Chen, and Tong He. FCOS: fully convolutional one-stage object detection. In *IEEE/CVF International Conference on Computer Vision (ICCV)*, 2019. 4
- [41] Tai Wang, Xinge Zhu, Jiangmiao Pang, and Dahua Lin. FCOS3D: fully convolutional one-stage monocular 3d object detection. In *IEEE/CVF International Conference on Computer Vision Workshops (ICCVW)*, 2021. 2, 6
- [42] Tai Wang, Xinge Zhu, Jiangmiao Pang, and Dahua Lin. Probabilistic and geometric depth: Detecting objects in perspective. In *Conference on Robot Learning (CoRL)*, 2021. 6
- [43] Yan Wang, Wei-Lun Chao, Divyansh Garg, Bharath Hariharan, Mark E. Campbell, and Kilian Q. Weinberger. Pseudo-lidar from visual depth estimation: Bridging the gap in 3d object detection for autonomous driving. In *IEEE/CVF Conference on Computer Vision and Pattern Recognition (CVPR)*, 2019. 2
- [44] Yue Wang, Vitor Guizilini, Tianyuan Zhang, Yilun Wang, Hang Zhao, and Justin Solomon. DETR3D: 3d object detection from multi-view images via 3d-to-2d queries. In *Conference on Robot Learning (CoRL)*, 2021. 3, 6
- [45] Tianwei Yin, Xingyi Zhou, and Philipp Krähenbühl. Center-based 3d object detection and tracking. In *IEEE/CVF Conference on Computer Vision and Pattern Recognition (CVPR)*, 2021. 6
- [46] Feihu Zhang, Victor Adrian Prisacariu, Ruigang Yang, and Philip H. S. Torr. Ga-net: Guided aggregation net for end-to-end stereo matching. In *IEEE/CVF Conference on Computer Vision and Pattern Recognition (CVPR)*, 2019. 2
- [47] Renrui Zhang, Han Qiu, Tai Wang, Xuanzhuo Xu, Ziyu Guo, Yu Qiao, Peng Gao, and Hongsheng Li. Monodetr: Depth-aware transformer for monocular 3d object detection. *CoRR*, 2022. 2, 4, 6
- [48] Yunpeng Zhang, Jiwen Lu, and Jie Zhou. Objects are different: Flexible monocular 3d object detection. In *IEEE/CVF Conference on Computer Vision and Pattern Recognition (CVPR)*, 2021. 2
- [49] Yunpeng Zhang, Zheng Zhu, Wenzhao Zheng, Junjie Huang, Guan Huang, Jie Zhou, and Jiwen Lu. Beverage: Unified perception and prediction in birds-eye-view for vision-centric autonomous driving. *CoRR*, 2022. 1
- [50] Zixiang Zhou, Xiangchen Zhao, Yu Wang, Panqu Wang, and Hassan Foroosh. Centerformer: Center-based transformer for 3d object detection. In *European Conference on Computer Vision (ECCV)*, 2022. 3
- [51] Benjin Zhu, Zhengkai Jiang, Xiangxin Zhou, Zeming Li, and Gang Yu. Class-balanced grouping and sampling for point cloud 3d object detection. *CoRR*, 2019. 6
- [52] Xizhou Zhu, Weijie Su, Lewei Lu, Bin Li, Xiaogang Wang, and Jifeng Dai. Deformable DETR: deformable transformers for end-to-end object detection. In *International Conference on Learning Representations (ICLR)*, 2021. 3, 5, 7